Sensors and Actuators: A. Physical 334 (2022) 113334

Contents lists available at ScienceDirect

Sensors and Actuators: A. Physical

journal homepage: www.elsevier.com/locate/sna

Fluid compressional properties sensing at microscale using a longitudinal bulk acoustic wave transducer operated in a pulse-echo scheme

Jesus Yanez, Arantxa Uranga, Nuria Barniol*

Department of Electronics Engineering, Universitat Autònoma de Barcelona, 08193 Bellaterra, Spain

ARTICLE INFO

Article history:
Received 16 August 2021
Received in revised form 25 November 2021
Accepted 21 December 2021
Available online 23 December 2021

Keywords:
Piezoelectric
AlN
Bulk acoustic wave
Ultrasonic microsensors
HBAR
Pulse-echo
Time-of-flight
Microfluidics

ABSTRACT

Acoustic devices have been widely used as smart chemical and biochemical sensors since they are sensitive to mechanical, chemical, optical or electrical perturbations on their surfaces; making them a reliable option for noninvasive detection of changes in physical properties of liquid samples for real-time applications. Here we present a longitudinal acoustic wave device for study of compressional properties of liquids in microfluidic systems, with the particularity of pulse-echo mode of operation. We have studied at a microscale the interaction between longitudinal acoustic waves and the compressional properties of liquid samples, interrogating the fluids with short pulses of ultrasound at GHz, finding a direct relationship between the magnitude of the bulk modulus or the specific acoustic impedance of liquids and the amplitude of the output voltage produced by acoustic echoes received by the aluminum nitride transducer. Analytical expressions and FEM simulations support the detection mechanism, while applications such as classification of liquids and detection of concentration change in solutions experimentally demonstrate the method. This contribution overcomes current restrictions of film acoustic resonators such as fragility of operation in liquid environments, high manufacturing cost or limitations regarding narrow microchannels; offering an alternative to applications that demand ultra-low consumption, miniaturization, versatility (it offers multi-frequency operation in 1 – 10 GHz range) and ease of readout (peak voltage).

1. Introduction

Body fluids such as blood or urine are an attractive source of information for disease detection [1–4], and one of the techniques for track their condition is by monitoring their mechanical properties [5–7], among which are its compressional properties. Compressional information is an interesting parameter in analysis since, at microscales, it is closely related to the chemical bond strength between atoms, ions, or molecules, and therefore can be used in analyzing human physiological fluids [8,9]. For instance a change in the mechanical properties of blood can be potentially related with cardiovascular dysfunctions, providing a fast and simple method for rapid and early test of a possible disease as it is already explained in reference [5]. Among the existent microscale biosensing technologies for liquid phase measurement, the acoustic wave methods are popular since they are noninvasive, passive and offer high sensitivity; acoustic transducers such as the quartz crystal microbalance (QCM), the surface acoustic devices (SAW) or the bulk acoustic resonators (BAR) have demonstrated their potential use as biosensors because they are sensitive to mechanical, chemical or electrical perturbations on their surfaces [10,11], these microsensors offer high resolution sensing of temperature, moisture, strain, pressure, shock, acceleration, flow, viscosity, and magnetic or electric fields, while offering a low cost solution with simple operation and readout integration. Despite the relative maturity of acoustic wave technologies such as QCM or SAW, thin-film bulk acoustic resonators (FBAR) are extensively studied since they are several orders of magnitude smaller than the former, allowing reduction of manufacturing cost and miniaturization, which is an advantage for its integration in Lab-on-a-Chip devices (LoC) [12].

FBARs consist of a piezoelectric layer sandwiched between two thin conductive electrodes; when the thickness extensional mode of the active layer is excited it generates and traps acoustic energy within its thickness. The resonance frequency of such devices, typically in the GHz order, depends on both the thickness and sound velocity of longitudinal waves of the piezoelectric film [13], offering higher sensitivity and increased resolution compared to other acoustic resonators; however, these thin released structures suffer from low yield due to residual stress and their use as biosensors for

* Correspondence to: Department of Electronics Engineering, Escola d'Enginyeria, Building Q, Office: QC-3045, 08193 Bellaterra, Spain.
E-mail address: nuria.barniol@uab.cat (N. Barniol).

https://doi.org/10.1016/j.sna.2021.113334
0924-4247/

liquid media is limited because tend to be brittle (trench-type and the air-gap-FBARs) [14]. Energy confinement in the thin-film piezoelectrical layer can be also achieved using Bragg-mirror-type FBARs, known as solid mounted resonators (SMR) [15]; such transducers offer improved mechanical robustness but require multiple precisely controlled deposition steps for the acoustic mirrors, raising the cost of the device and causing its performance to be dependent on manufacturing defects [16]. A similar approach that addresses the aforementioned disadvantages are the High-Overtone Bulk Acoustic Resonators (HBARs) used as sensors [17]; in this case the piezoelectric and its electrodes are deposited directly on an acoustic substrate offering both, a robust structure and simpler manufacturing. Unlike FBAR or SMR devices, HBAR structures allow leakage of acoustic energy into the wafer, generating stationary bulk acoustic waves in the substrate thickness, therefore the free face of the wafer (the opposite of where the piezoelectric layer and its electrodes were patterned) can be used as a detecting surface totally free of electronics [18], which is an attractive feature for microfluidics carrying conductive or non-conductive liquids.

Here we present an HBAR microstructure, operating in a pulse-echo scheme, for studying compressional properties of liquids in real-time applications. Rather than the elaborated mechanisms for signal control and measurement used in acoustic resonators (which consist of detecting changes in amplitude and frequency shift of resonance peaks in the impedance curve caused by modifying the acoustic load coupled to the resonator [9,18–22]), this pulse-echo scheme only requires measurement of the peak voltage produced by an acoustic echo within a determined time-of-flight (ToF) [23,24]. The transducer presented here allows multiple operating frequencies in the 1–10 GHz range, offering a low-power solution for monitoring compressional properties of fluids in microchannels where the active detection area and depth of penetration of ultrasound in liquid samples are critical.

2. Principle of operation and FEM simulations

2.1. Detection mechanism and system description

In this work, the microscale measurement of compressional properties of liquids is based on the interaction between pulses of longitudinal acoustic waves traveling across the solid sensor to the liquid sample and the opposition exerted by such fluid to acoustic flow (its acoustic impedance). The complex acoustic impedance of materials Z^* is related to density ρ and the dynamic complex modulus M^* (ω) as [25]:

$$Z^* = \sqrt{\rho M^*(\omega)} \tag{1}$$

With $\omega = 2\pi f$ as the angular frequency. For longitudinal waves, M^* is a function of the complex compressibility modulus (Bulk modulus) K^* and the shear modulus G^*[25]:

$$M^*(\omega) = K^*(\omega) + \frac{4}{3}G^*(\omega)$$

The complex modulus K^* is stated as $K^* = K' + iK''$ [51], where K' is the storage modulus representing the elastic part and K'' is the loss modulus, representing the viscous part. Similarly for the shear modulus G^* we have $G^* = G' + iG''$, with G' as the shear storage modulus and G'' as the shear loss modulus. For Newtonian media the shear modulus G^* can be reduced to its imaginary part $G^* \approx iG''$ [52], so that the dynamic modulus of the liquid for longitudinal waves is:

$$M^*(\omega) = K' + iK'' + i\frac{4}{3}G''$$

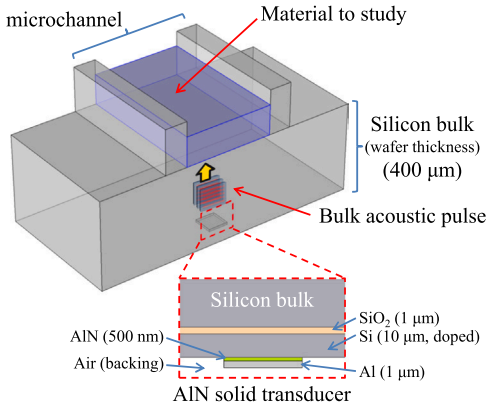

Fig. 1. A 3D transparent slice representing the concept of the sensor: The lower face of the wafer carries the transducer that emits and receives pulses of bulk waves through the thickness of the wafer while the upper face remains free of electronics and cables and is used as a detection surface carrying liquid samples. The zoomed section is a 2D representation of the stack of materials that make up the transducer; the piezoelectric material is AlN, sandwiched between conductive materials for excitation of thickness extensional modes. Thicknesses and materials correspond to the PiezoMUMPs multi-user process.

The loss moduli K'' and G'' are respectively related to compressional and shear viscosities as: $\mu_B = K''/\omega$ and $\mu = G''/\omega$ [52,53], where μ_B is the real part of the bulk viscosity and μ is the real part of the shear viscosity. Thus, the dynamic modulus of a liquid subjected to a longitudinal compressive force:

$$M^*(\omega) = K' + i\omega\left(\mu_B + \frac{4}{3}\mu\right) \tag{2}$$

In the case of liquids, the real part of the bulk modulus K' is related to the speed of sound c as $K' = \rho c^2$. Therefore, substituting Eq. 2 in Eq. 1, the complex acoustic impedance of a liquid subjected to a pressure wave is [9,26]:

$$Z_{liquid} = Z_{real}\sqrt{\left[1 + i\frac{\omega}{\rho c^2}\left(\mu_B + \frac{4}{3}\mu\right)\right]}$$

$$Z_{real} = \rho c \tag{3}$$

The latter indicates that compressional information such as the Bulk Modulus and the specific Acoustic Impedance can be obtained by interrogating a liquid sample with pulses of longitudinal waves produced by a transducer. To ease the interaction between liquid samples and the transducer at microscales we use the sensor described by Fig. 1, where one face of the wafer carries an AlN piezoelectric layer emitting and receiving ultrasound pulses and the opposite face, which is a bare silicon surface with no electronics or wires, is enabled to implement microchannels carrying either conductive or non-conductive liquids. Materials and thicknesses in Fig. 1 correspond to the PiezoMUMPs multi-user process [27], by MEMSCAP.

Rather than operate this HBAR as a resonator, we drive its piezoelectric element with a short RF pulse to excite thickness extensional modes. In consequence a short ultrasound pulse of bulk waves travels across the thickness of the substrate and it interacts with the liquid sample in the opposite face of the wafer. The Time-of-Flight (ToF) needed for the ultrasound pulse is $ToF = h_{subs}/c_{subs} = 48$ ns; considering $h_{subs} = 411$ µm as the total thickness of the stack and $c_{subs} = 8457$ m/s as the reported sound velocity of longitudinal waves in silicon. The acoustic impedance discontinuity at the solid-liquid

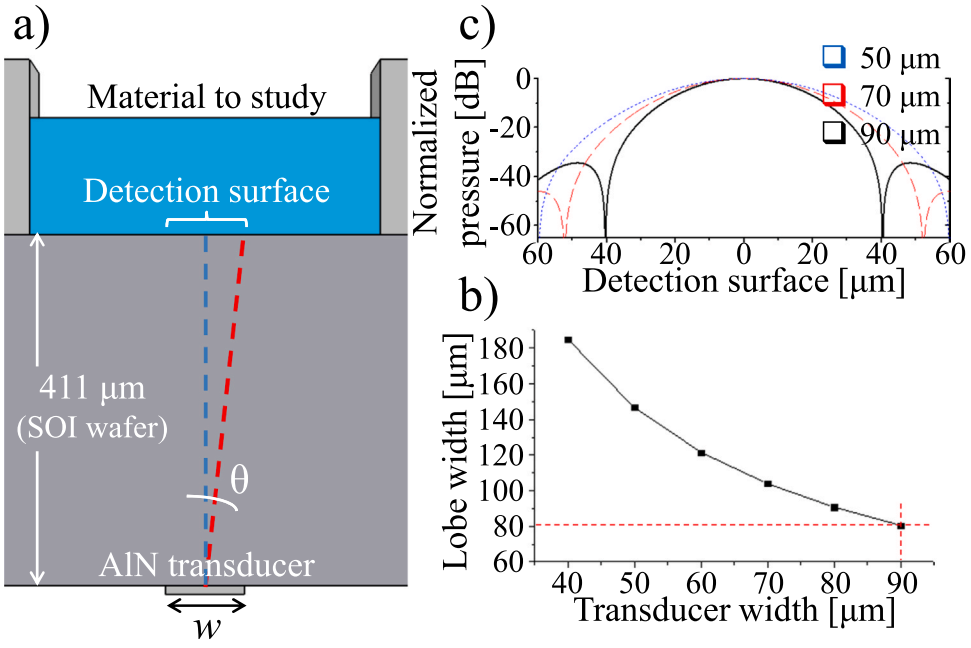

Fig. 2. Acoustic pressure distribution at the detection surface for transducers of different width (50 µm, 70 µm and 90 µm). a) Cross-section schematic of the sensor. b) Lobe-width defined by the main-lobe pressure as a function of transducer width. c) Normalized pressure showing the size of pressure lobes at the detection surface. Computed at 1 GHz.

interface causes a part of the pulse to be reflected back towards its emitting piezoelectric element, which provides a method to determine Z_{liquid} by measuring the amount of acoustic energy reflected. If diffraction losses, damping and scattering are negligible, the amount of energy reflected in at the detection surface is [28]:

$$|\Gamma| = \frac{|Z_{liquid} - Z_{substrate}|}{Z_{liquid} + Z_{substrate}} \tag{4}$$

With $Z_{substrate}$ as the acoustic impedance of the substrate (silicon, in our device). In this approach, the acoustic energy reflected towards its source is converted back to an electrical signal by the inverse piezoelectric effect. The amplitude of the output voltage is then proportional to the specific acoustic impedance Z_{liquid} of each liquid.

2.2. Microsystem design and acoustic pressure distribution at the detection surface

In this scheme the same single-element transducer is responsible for both transmission and reception of ultrasound pulses interacting with the material to be studied; therefore, it is convenient to minimize diffraction of the acoustic energy during its travel across the thickness of the wafer. For the far field case, the width of the ultrasound pulse at the detection surface could be estimated with the condition $w\sin\theta = \lambda$, where w is the width of the transducer, θ the angle formed between the central axis of Fig. 2a and the point in the detection interface where the minima of the main lobe will appear, and λ is the wavelength of the longitudinal ultrasound wave traveling in the substrate, which is related to the operating frequency f_{op} as $\lambda = c_{subs}/f_{op}$. An HBAR structure consisting of a 0.5 µm-thick AlN piezoelectric layer over a 400 µm-thick silicon exhibits multiple resonant modes separated by Δf = 11 MHz ($\Delta f = c_{subs} / [2 * h_{subs}]$) in a comb profile, modulated by the piezoelectric resonance f_0 at 10.9 GHz ($f_0 = c_{piezo} / [2 * h_{piezo}]$, where c_{piezo} = 10,900 m/s, and h_{piezo} = 0.5 µm) [29]. The configuration of materials surrounding the piezoelectric layer (zoomed section in Fig. 1), leads to additional modulation of the frequency comb, causing appearance of multiple resonating modes with increased electromechanical coupling in the 1–10 GHz range [34]. Therefore, if we set 1 GHz as the lowest operating frequency and the detection surface is 411 µm far from the transducer, it is found by $w\sin\theta = \lambda$ that a value of w between 80 and 90 µm corresponds to the narrowest transducer that can be used avoiding diffraction at that operating frequency, i.e., the width of the main lobe at the detection surface will be similar to the width of the emitting transducer (Fig. 2b). Fig. 2c show the normalized pressure distribution at the detection surface caused by transducers of different widths operating at 1 GHz; this 2D pressure distribution in the far field was analytically obtained from (5) [30], plotting only distribution along θ.

$$p(r, \theta, \varphi, t) = j\frac{kcu_a\rho w^2}{2r\pi}\frac{\sin(\alpha)}{\alpha}\frac{\sin(\beta)}{\beta}e^{[j(\omega t - kr)]} \tag{5}$$

$$\alpha = (kw\sin\theta\sin\varphi)/2$$

$$\beta = (kw\sin\theta\cos\varphi)/2$$

Where k is the wavenumber, c is the sound velocity in silicon, u_a is the transducer vibration velocity, ρ is the medium density, w is the width of the squared transducer, ω is the angular frequency and r is the distance from the transducer to the point to evaluate $P(\theta)$.

Through time-dependent Finite Element (FEM) simulations (COMSOL) we verify the acoustic pressure distribution at the sensing surface. For t = 50 ns (Fig. 3a) the acoustic pulse has already traveled through the thickness of the substrate and has reached the detection surface. This pressure distribution plot confirms low diffraction of the acoustic pulse emitted by a squared transducer of width w = 90 µm and the expected ToF = 48 ns. The pressure distribution plot in Fig. 3b exemplifies the detection mechanism at t = 72 ns, when part of the acoustic energy has been transferred to the liquid media

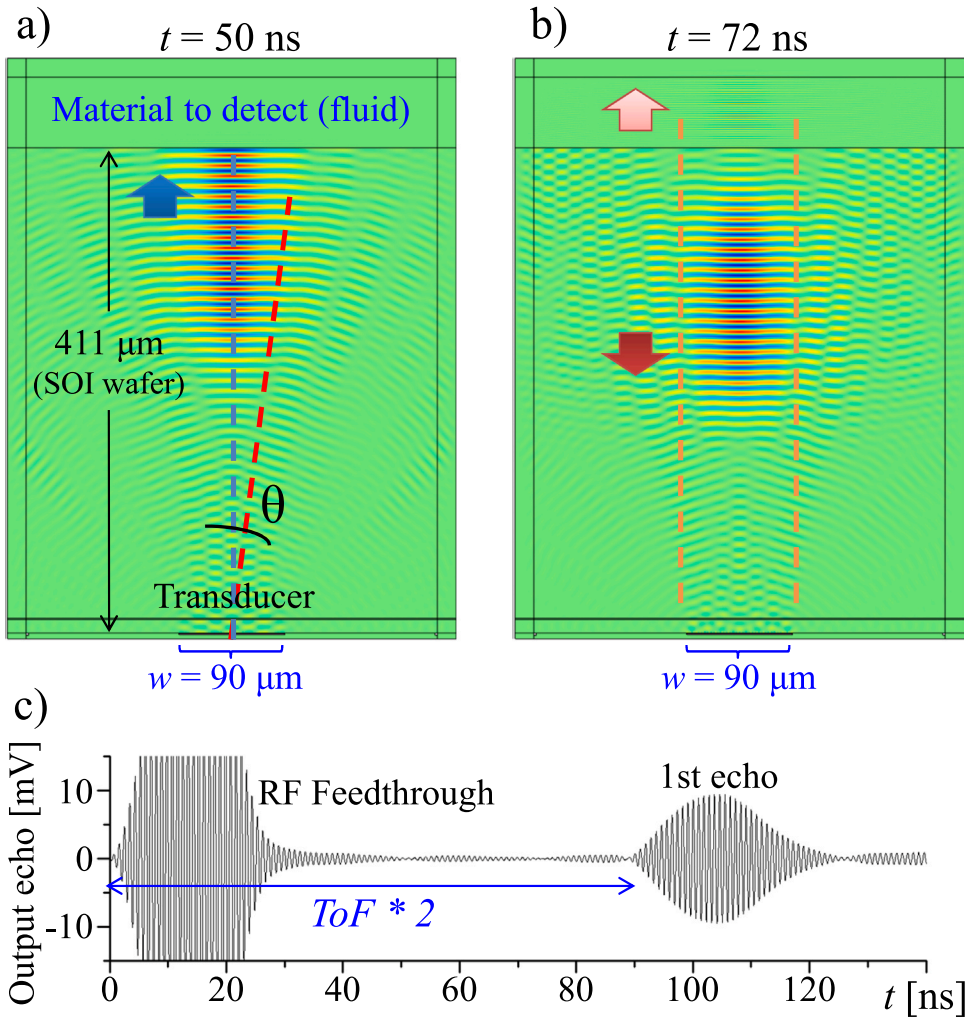

Fig. 3. Time dependent simulation of the evolution of the ultrasound pulse emitted by the w = 90 µm transducer working at 1 GHz showing low diffraction of the acoustic energy: a) Transmitting pulse, b) Echo pulse. c) Time response plot of output voltage signal produced by the received acoustic echo at t > 90 ns (corresponding to ToFx2).

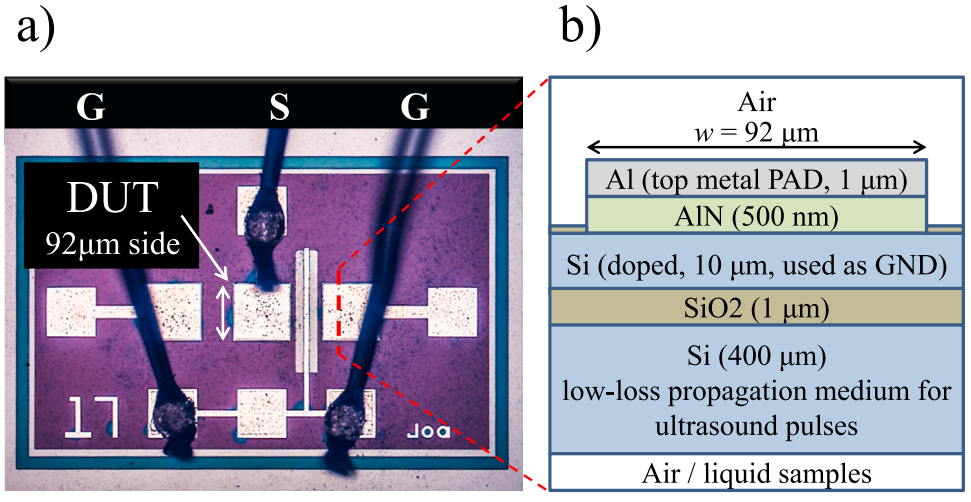

Fig. 4. a) Optical image of a manufactured 1-D linear array consisting of three HBAR structures, each square transducer is 92 µm wide, only the central element is connected to the drive & read circuit. b) Cross section profile of the stack of materials used to fabricate the HBAR structure (Cross section representation is not to scale and it is flipped with respect to Fig. 1 to correspond with Fig. 4a, where the top layer is the metal PAD).

Table 1
Properties of the materials forming the stack of the manufactured device. Quantities correspond to default values from COMSOL library and their respective acoustic impedance is obtained by the approximation $Z \approx \rho c_{mat}$, with c_{mat} as the sound velocity of each material.

Material	h [μm]	ρ [kg/m^3]	c_{mat} [m/s]	$Z \approx \rho c_{mat}$ [Rayl]
Air		1.14	349.1	398
Al	1	2700	6450	17.415E+6
AlN	0.5	3300	10954	36.148E+6
Doped Si	10 ± 1	2329	8457	19.696E+6
SiO2	1	2200	5848	12.866E+6
Si < 100 >	400 ± 5	2329	8457	19.696E+6

and it continues its flight in the direction indicated by the pink arrow, meanwhile, the complementary portion of the emitted acoustic energy was reflected back towards the emitter (red arrow). The voltage plot in Fig. 3c (FEM simulation) shows the output signal produced by the received acoustic echo at $t > 90$ ns; the amplitude of the output voltage will be proportional to Z_{liquid} according to Eq. 4.

3. Fabrication and operating frequencies

3.1. Fabrication

This sensor was manufactured using the PiezoMUMPs multi-user process from MEMSCAP [27]. The transducer consists of a 0.5 μm thick AlN layer patterned over a Silicon-On-Insulator wafer (SOI), and its metal electrode for drive and read-out purposes. The side of the wafer carrying the AlN layer is 10 ± 1 μm of silicon superficially doped, used here as reference to ground, allowing the piezoelectric to operate in its thickness extensional mode [31]. The remaining thicknesses are 1 μm of SiO_2 and 400 ± 5 μm of crystalline silicon, which is our lossless propagation medium for the ultrasound pulses. This process leads us to the 1-D linear array of HBARs shown in Fig. 4a; according to the purposes of this document, only the central transducer (the device under test, DUT) is connected to the drive & read circuitry. Fig. 4b is a cross section representation of the stack of materials used to fabricate the HBAR structure, this cross section representation is not to scale.

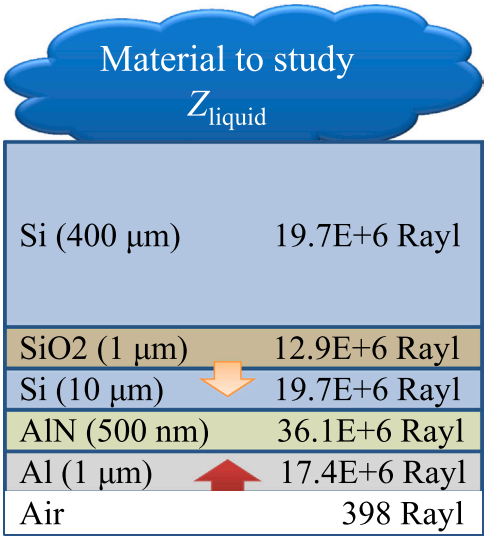

Fig. 5. Thickness and acoustic impedance of materials surrounding the piezoelectric layer.

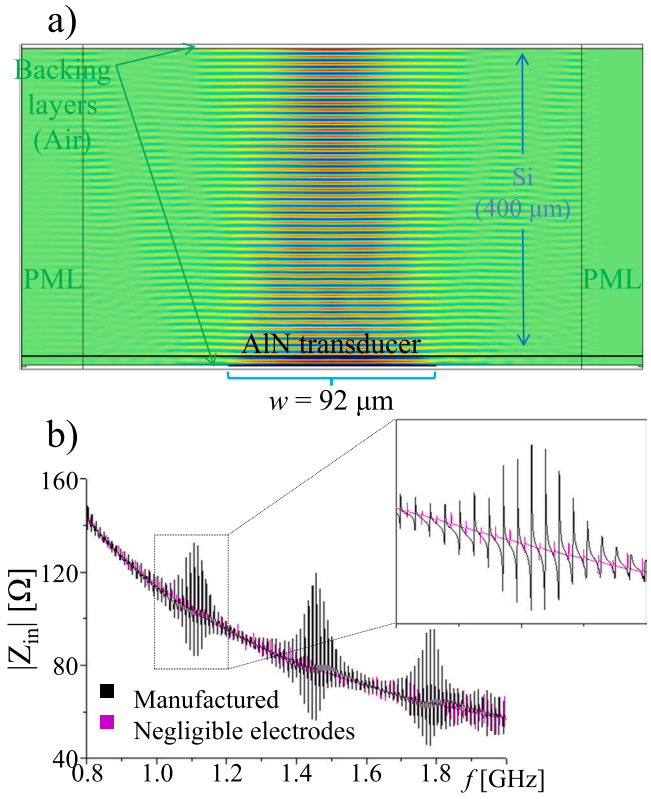

Fig. 6. a) 2D model for frequency-domain FEM simulations, illustrating the confinement of acoustic energy caused by a continuous low-power RF source in an HBAR with dimensions corresponding to materials and thicknesses of the manufactured device. b) Input electrical impedance plot as result of frequency domain simulations in the 0.8–2 GHz region; the configuration of layers and materials constituting our bulk acoustic transducer cause modulation of the frequency comb.

3.2. Operating frequency

The resonating frequency of a thin piezoelectric layer operating on its thickness expansion mode is given by $f_r = c_{piezo}/2h_{piezo}$, with c_{piezo} as the sound velocity of longitudinal waves in the piezoelectric material and h_{piezo} as its thickness [31]. When this film is deposited on an acoustic substrate, bulk acoustic waves are generated and keep trapped in the thickness of the whole stack. If the substrate thickness $h_{subs} > > h_{piezo}$, then the fundamental mode of the structure is $f_0 \approx c_{subs}/2h_{subs}$ (with c_{subs} as the sound velocity of the substrate). The electrical response of such structure is a comb formed by the multiple harmonics of the fundamental mode of the structure, separated by Δf_0 [32]. For this two-layer device the amplitude of the comb of substrate modes is modulated by the resonance of the piezoelectric. Table 1 lists material properties and thicknesses h_{mat} of materials forming the fabricated device.

According to values of Table 1, the magnitude of the electrical response of our device is a comb of resonances separated by $\Delta f_0 = 11$ MHz, modulated by the piezoelectric resonance at $f_r = 10.9$ GHz. The above allows formation of stationary bulk acoustic waves of $\lambda < 10$ μm for operating frequencies above 1 GHz, therefore, the influence of the thickness of the different materials surrounding the AlN layer is not negligible [31,33]. Fig. 5 shows thicknesses and acoustic impedance of the different materials surrounding the piezoelectric; since the acoustic impedance of these solid materials is the same order of magnitude as that of the AlN film, it is expected

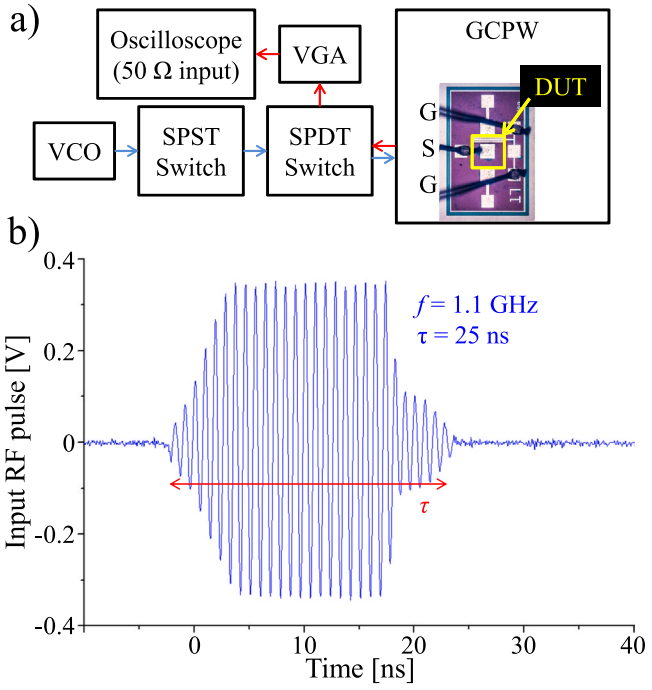

Fig. 7. a) Schematic of the experimental set-up. b) Characteristics of the excitation RF pulse.

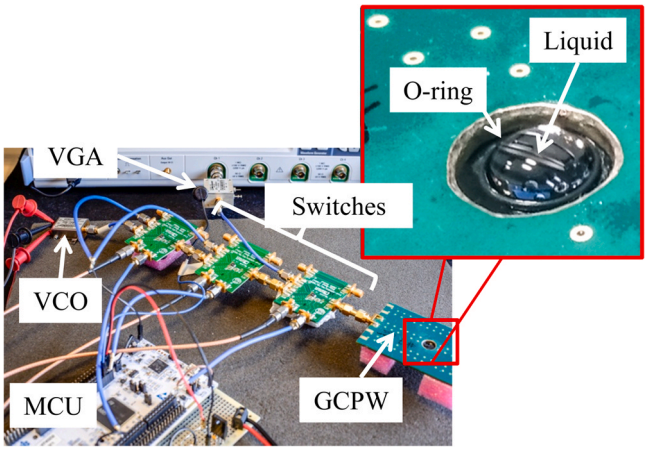

Fig. 8. Optical image of the experimental setup.

that the acoustic energy generated by exciting the thickness extension mode of the piezoelectric will be transferred to these materials causing multiple acoustic reflections.

In Fig. 5 the Al electrode is twice as thick as the piezoelectric and both materials have similar acoustic impedance, therefore, the mechanical energy produced by the piezoelectric is immediately transferred to this thicker layer and then is reflected back towards the piezoelectric (red arrow) because of the huge acoustic impedance difference with 'air' in the lower boundary. In the opposite side, partial reflection of the longitudinal wave is induced by the mismatch between acoustic impedances of the doped silicon and buried oxide. To investigate the influence of these reflections in the transfer function of the device we use the 2-D Frequency-domain FEM simulation of Fig. 6a. The impedance plot in Fig. 6b compares the magnitude of the input electrical impedance Z_{in} for a transducer as manufactured (black trace) respect to the transfer function of a similar device but electrodes of negligible thickness (magenta), for the frequency range 0.8–2 GHz.

As seen in the electrical impedance plot (Fig. 6b), the configuration of layers and materials constituting this bulk acoustic transducer cause additional modulation of the frequency comb. These frequency spots with higher amplitude modes also offer a significant increase in the effective electromechanical coupling k^2_{eff} [34], improving transduction of our pulse-echo devices and providing them with multi-frequency capability. For the sake of simplicity, here we have used the peak of transduction located at 1.1 GHz for the experimental part.

4. Experimental part and discussion

The device under test (DUT) is the squared transducer with side w = 92 µm shown in Fig. 4a, this device is wire bonded to a 50 Ω Grounded Coplanar Waveguide (GCPW) with an SMA connector to interact with the excitation/read circuit. The schematic in Fig. 7a describes the electronic components used to drive and read the sensor. It starts with a Voltage Controlled Oscillator (VCO) ZX95–1750 W-S+ generating a 1.12 GHz continuous RF signal (6 dBm), then a Cortex-M7 microcontroller activate both the SPST Switch (ADG901) and the SPDT switch (ADG918) allowing to pass a short RF pulse of duration τ = 25 ns as the shown in Fig. 7b. Once the ultrasound pulse has been emitted the microcontroller returns the SPDT switch to its original position allowing the voltage signal produced by the reflected echoes to pass through the Variable Gain Amplifier (VGA) ZFL-1200 G+ (gain 25.8 dB @1.1 GHz), the output signal is retrieved by the 50 Ω input of the oscilloscope Rohde& Schwarz RTO2064. Since one face of the chip carries the transducer and the detection surface is at the opposite face, the GCPW is flipped upside down as it features a hole exposing the detection surface (bare silicon) to place liquid samples. Samples are delivered with a transfer pipette (sample ~ 50 µL) and confined with an o-ring (Fig. 8).

As speed of sound in materials changes with temperature, leading to deviations of acoustic impedance, we take measurements of the reflection coefficient (silicon/liquid interface) at the same room temperature for all liquid samples. The following experiments were performed to verify sensitivity to both Bulk Modulus and Acoustic Impedance of tested materials and to determine how they are related to the amplitude of the output voltage signals: a) Ability to detect the presence of liquid on the detection surface and feasibility of application as a biometric fingerprint sensor, b) Identification and classification of liquids by their specific acoustic impedance, and c) Detection of concentration change in solutions (with different mixtures of glycerol and water). Table 2 lists properties of the liquids used in the experimental part and their expected reflection coefficient Γ calculated by Eq. (4). Due to the relative high viscosity of glycerol and the interaction with pressure acoustic waves at GHz, the frequency-dependent value of its acoustic impedance (Eq. 3) is also included.

4.1. Presence of liquids in microchannels and impedance imaging (fingerprint sensor)

To test the capability of this all-solid sensor to identify if a microchannel is filled with liquid or not, we record the output voltage produced by echoes reflected from the detection surface for both, when there is liquid on the detection surface and when it is free.

Table 2
Properties of liquids analyzed (values obtained from literature [35–46]).

Material 31 °C	Density ρ [kg/m^3]	Acoustic velocity c [m/s]	Viscosity μ [cP]	Bulk modulus $K' = \rho c^2$ [GPa]	Acoustic impedance $Z \approx \rho c$ [Rayl]	Γ (Eq.4)
Air	1.14[35]	349.1[36]	0.018[35]	1.3893E-04	398	0.9999
Ethanol	780.1[37]	1105.7[38]	1.06[39]	0.9537	0.8625E+06	0.9161
FC-70	1924[40]	680[41]	3.36[40]	0.8896	1.3083E+06	0.8754
DI Water	995.6[42]	1511.4[43]	0.79[44]	2.2743	1.5047E+06	0.8580
Glycerol	1254[45]	1902[46]	552.1[45]	4.5364	2.3851E+06	0.7839
					Acoustic impedance $Z(\omega)$,Eq. 3 [Rayl]	
Glycerol* @ 1.1 GHz	1254	1902	552.1		3.2239E+06	0.7186

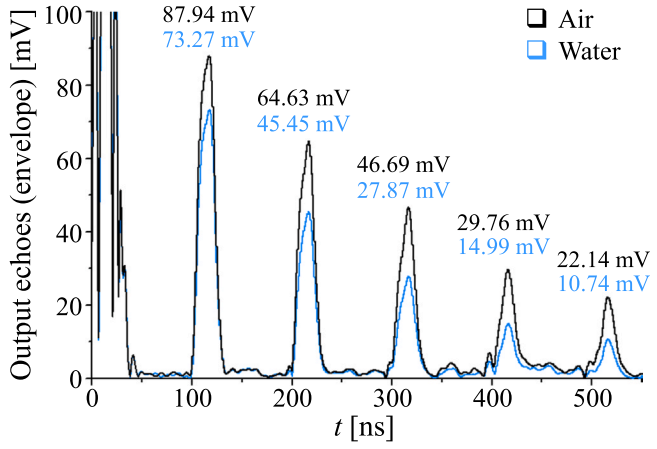

Fig. 9. Envelope of five consecutive echoes for the case of "air" on the detection surface (black) and envelope for the case of "water" (blue).

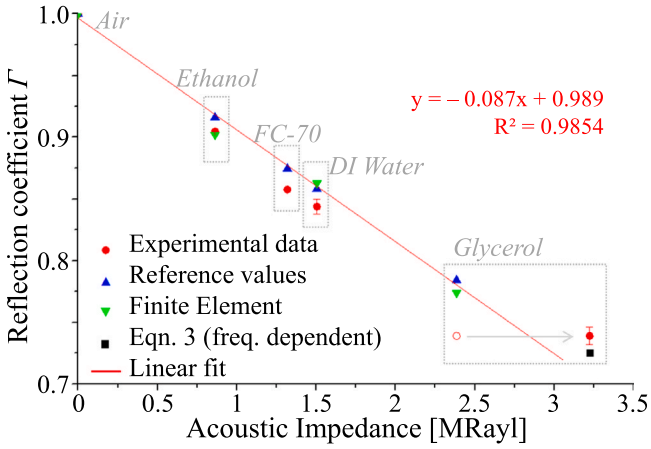

Fig. 10. Reflection coefficient obtained from measurements and related to the specific acoustic impedance of each substance. Due to the viscosity of glycerol (> 500 cP), a frequency-dependent acoustic impedance value (Eq. 3) has also been added.

Fig. 9 presents the envelope of output signal recorded by the oscilloscope, up to $t = 550$ ns, after applying one input RF pulse for the case of both, no material filling the o-ring, and filled with deionized water.

Fig. 9 showed a first echo rising up to 38 dB above the noise floor and the time-of-flight is according with the expected value ToF(x2) ≈ 96 ns (for a round trip across the thickness of the wafer). This echo is followed by multiple remaining echoes of lower amplitude with same ToF since the side of the wafer carrying the transducer is also in contact with air, causing total reflection of the acoustic energy and therefore interaction with the material to be studied more than once while the pulse gradually fades with time. Considering only the first echo we notice that the amplitude of the envelope corresponding to the case of distilled water (blue trace) drops close to 16% respect to the maximum amplitude obtained when the detection surface is cleared (air, black trace), which agrees to the theoretical reflection coefficient differences in Table 2, demonstrating ease of detection as long as the 'air' signal is used as a reference.

Since acoustic impedance of skin is close to that of water, an array of these transducers can be used for imaging purposes (ultrasonic fingerprint sensors) by recording the difference in output voltage between zones of the sensing surface in contact with air (fingerprint valleys), and zones in contact with skin (fingerprint ridges) [47]. As seen in Fig. 9, each pulse reflection (round trip) increases the difference between the envelope caused by 'water' and the caused by 'air' (because acoustic energy leakage into the liquid on each interaction), therefore, enhanced contrast can be obtained at the cost of increasing acquisition time. We use the fourth echo ($t = 400$ ns, SNR ~ 20 dB) to indicate contrast between echoes reflected by water (acting as a fingerprint ridge) respect to echoes reflected by the cleared sensor (acting as a fingerprint valley) in the

Table 3
Comparison against a similar transducer implemented as an imaging element (fingerprint sensor).

	[47], 2019	This transducer
Technology	AlN MEMS + 0.18 µm CMOS (monolithic)	AlN MEMS + Off the shelf electronics
Mode of operation	Pulse-echo	Pulse-echo
Elements required	2 (Transmitter + Receiver)	1 (Same element for Tx & Rx)
Drive voltage	> 1 V	< 0.4 V
Frequency	1.69 GHz	1.1 GHz (but possible for higher frequencies, up to 10 GHz
Contrast	2.3: 1	2: 1
Acquisition time	344 ns (Second echo)	400 ns (Fourth echo)

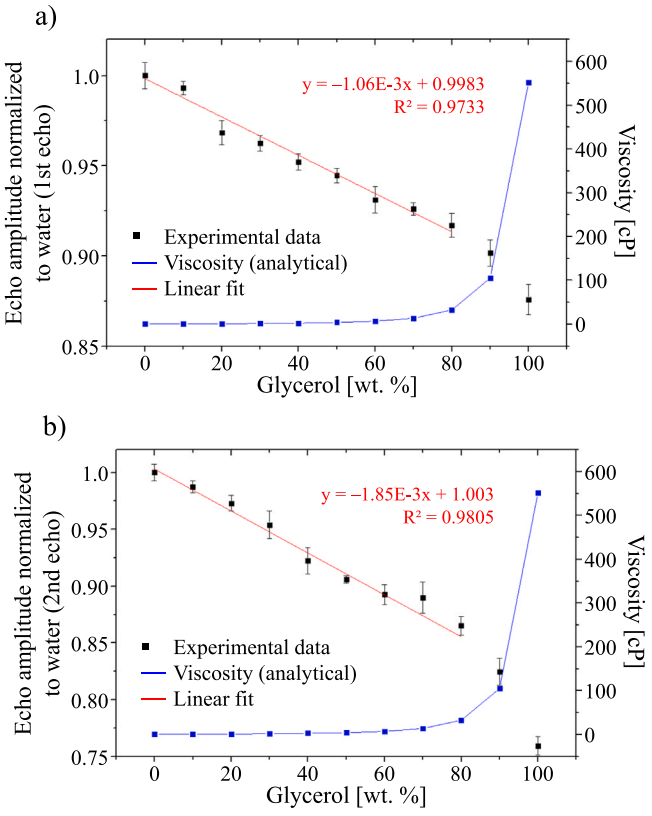

Fig. 11. a) Measured reflection coefficient as a function of glycerol content, using the first echo to detect changes in concentration. b) Measurements using the second echo.

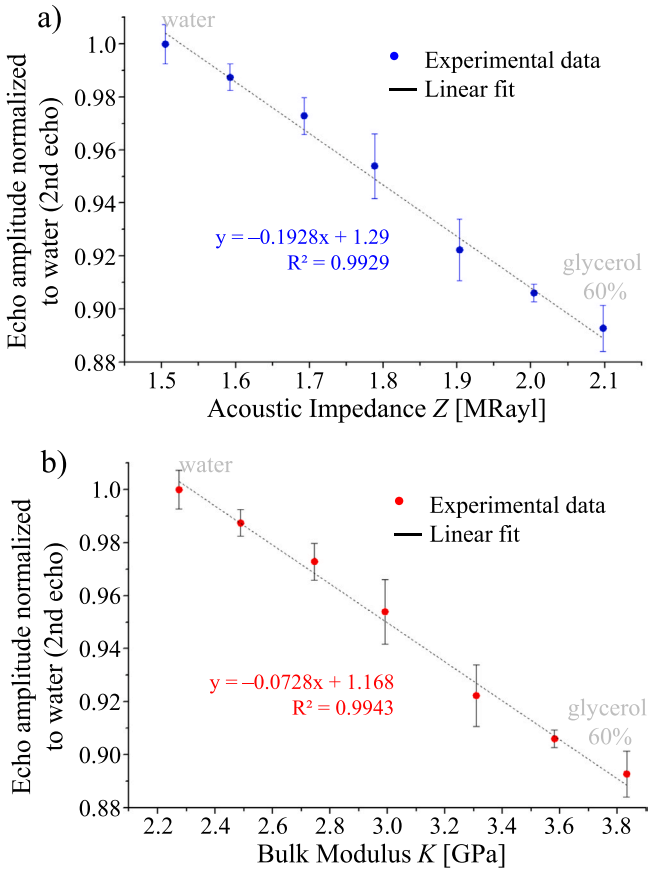

Fig. 12. Measured reflection coefficient of each glycerol concentration (0–60%), as a function of a) Reported Acoustic impedance b) Bulk modulus.

comparison of Table 3. Note that in this work only one single element is used both for Tx and Rx.

According to the diffraction condition $w\sin\theta = \lambda$, our approach with multi-frequency capability (up to 10 GHz) would allow single element transducers of width w = 25 µm sending low diffraction pulses of ultrasound to scan the detection surface with a lateral resolution of 30 µm, improving current ultrasonic sensors while offering very low drive voltage and low electrical input impedance (~150 Ω for such parameters).

4.2. Identification and classification of liquids by their specific acoustic impedance

Liquid substances in Table 2 exhibit dissimilar densities and longitudinal sound velocities, which offer opportunity of classification according to their degree of mismatch respect to the characteristic acoustic impedance of the silicon substrate transporting the pulses of longitudinal waves emitted by the piezoelectric element. Fig. 10 relates the values in Table 2 for reflection coefficient Γ with their respective acoustic impedance Z (reference values). In the case of experimental data, each reflection coefficient is obtained from the V_{liq}/V_{ref} relation, where V_{ref} is the voltage generated by received echoes when the detection surface is clear ('air' causes total reflection of the acoustic pulse and therefore a reference value), while V_{liq} is voltage generated in the case of each liquid (which depends on the amount of acoustic energy absorbed by each liquid).

As seen in Fig. 10, the reflection coefficient obtained from the measured output voltage of each liquid shows a linear relationship with the reference values for acoustic impedance. It is appreciated major dispersion for the measurement "glycerol", verifying that it should not be correlated neither with the acoustic impedance value

Table 4
Comparison to a reported resonating sensor of liquid bulk-modulus at microscales.

	[9], 2019	This transducer
Acoustic device type	SMR (FBAR)	HBAR
Mode of operation	Resonating	Pulse-echo
Sensitive area	0.01 mm²	0.008 mm²
Drive voltage	10 dBm (continuous)	4 dBm (25 ns pulse)
LAW frequency	2.5 GHz	1 – 10 GHz range
Liquid operation	Yes by passivation layer	Yes native
Parameter to detect	Change of resonant frequency	Voltage amplitude
Bulk modulus sensitivity	5.83 MHz / GPa	6.89% / GPa *

* Percentage change of reflection coefficient, taking water measurement as reference.

calculated from the approximation $Z \approx \rho c$ nor with the FEM result based on a simple linear elastic fluid model, but with the value obtained from Eq. 3, since the high viscosity of this material makes the frequency dependences relevant [48–50].

4.3. Detection of concentration change in solutions

We prepare glycerol/water mixtures (percentage by weight) to determine the ability to identify changes in concentration, demonstrate correlation between the output voltage of the sensor and bulk modulus *K*, and confirm lack of sensitivity to viscosity when studying biological fluids, where viscosity rarely exceeds 10 cP [48]. Each experimental point in Fig. 11a is the average value of five measurements performed at each concentration value (first echo), normalized to 'water' (0% glycerol). Measurements were performed at 31 °C (room temperature), so that the blue reference indicates the analytical value of the viscosity of each solution at that temperature [45]. Fig. 11b shows measurements of the second echo.

Fig. 11a shows that the level of acoustic energy absorbed by the liquid sample increases linearly (R2 > 0.97) as the concentration of glycerol in the mixture increases up to 80% (viscosity = 32.7 cP, at 31 °C [45]). From that point, experimental data show slight sensitivity to viscosity, when it increases its value above 32.7 cP (blue trace). If detection with the second echo is performed, the same behavior is observed, but for this case the pulse has interacted twice with the material to be detected, leading to a steeper calibration curve. Fig. 12a relates experimental measurements of Fig. 11b with their respective Acoustic Impedance value, obtained from literature [49], up to 60%. The values for Bulk Modulus in Fig. 12b were obtained from the same acoustic impedance data, using Eq. 3.

Fig. 12 indicates that the output voltage decreases 1.8% for each 100 kRayl increment in the acoustic impedance *Z*, and it decreases 6.9% per GPa in the case of changes in Bulk modulus *K*. This sensor shows high linearity for the measurement of these parameters ($R^2 > 0.99$, for both *Z* and *K*) as long as the viscosity of the solution does not exceed 10 cP as shown in Fig. 10 and Fig. 11, while further adjustments should be performed with liquid samples of much higher viscosity, such as pure glycerin, with a value above 500 cP at 31 °C. This sensor boasts application for biosensing in liquid media, where viscosity rarely exceeds 10 cP. Studies on compressional properties of liquids are mainly tackled by large-scale systems making it difficult to find direct competitors to compare; Table 4 compares our pulse-echo microsensor to a recently reported acoustic resonator based on SMR technology.

Despite sharing some characteristics such as similar dimensions of the active area or wavelength, our HBAR-based microsensor offers lower drive voltage with higher sensitivity, simpler manufacture and increased reliability respect to FBAR/SMR devices. In addition, its multi-frequency capabilities allow controlling penetration in liquids avoiding unwanted reflections in narrow channels or due to low sample volumes, which can also be discarded considering only signals received at the expected ToF. A very controllable RF pulse with finite length is chosen to avoid additional and non-desired echoes. Moreover, the pulse-echo mode of operation offers a much simpler drive/lecture method, where only output voltage amplitude should be recorded.

5. Conclusion

In this work we have presented a microsensor to study compressional properties of liquids in microfluidic systems by using longitudinal acoustic waves in a pulse-echo regime. Unlike FBAR approaches, this bulk acoustic structure is easy and inexpensive to manufacture, providing superior mechanical robustness and a sensing surface free of electronics where microchannels can be constructed carrying even conductive liquids. This device provides an alternative for noninvasive study of liquid samples at microscales; envisioned for real-time applications where low-power consumption, easy readout method and size matters.

Author contributions

Jesus Yanez: Conceived and designed the analysis, Collected the data, Performed the analysis, Wrote the paper. **Arantxa Uranga**: Contributed data or analysis tools, Other contribution (Revision). **Nuria Barniol**: Conceived and designed the analysis, Contributed data or analysis tools, Wrote the paper, Other contribution (Revision).

Declaration of Competing Interest

The authors declare that they have no known competing financial interests or personal relationships that could have appeared to influence the work reported in this paper.

Acknowledgments

This research was partially funded by the Spanish Ministry of Science and Innovation, with project PID2019-108270RB-I00.

References

[1] I.J. Miller, S.R. Peters, K.A. Overmyer, B.R. Paulson, M.S. Westphall, J.J. Coon, Real-time health monitoring through urine metabolomics, npj Digit. Med. 2 (2019) 109, https://doi.org/10.1038/s41746-019-0185-y
[2] J.J. Coon, P. Zürbig, M. Dakna, A.F. Dominiczak, S. Decramer, D. Fliser, M. Frommberger, I. Golovko, D.M. Good, S. Herget-Rosenthal, J. Jankowski, B.A. Julian, M. Kellmann, W. Kolch, Z. Massy, J. Novak, K. Rossing, J.P. Schanstra, E. Schiffer, D. Theodorescu, R. Vanholder, E.M. Weissinger, H. Mischak, P. Schmitt-Kopplin, CE-MS analysis of the human urinary proteome for biomarker discovery and disease diagnostics, Prot. Clin. Appl. 2 (2008) 964–973, https://doi.org/10.1002/prca.200800024
[3] M. Li, Urine reflection of changes in blood, in: Y. Gao (Ed.), Urine Proteomics in Kidney Disease Biomarker Discovery, Advances in Experimental Medicine and Biology, 845 Springer, 2015, pp. 13–19, https://doi.org/10.1007/978-94-017-9523-4_2
[4] Wu Jianqiang, Youhe Gao, Physiological conditions can be reflected in human urine proteome and metabolome, Expert Rev. Proteom. 12 (2015) 623–636, https://doi.org/10.1586/14789450.2015.1094380
[5] Hye Jin Kim, Kim Jinsik, Zandieh Omid, Myung-Sic Chae, Tae Song Kim, Jeong Hoon Lee, Jung Ho Park, Seonghwan Kim, Kyo Seon Hwang, Piezoelectric layer embedded-microdiaphragm sensors for the determination of blood viscosity and density, Appl. Phys. Lett. 105 (2014) 153504, https://doi.org/10.1063/1.4898637
[6] K. Roy, H. Gupta, V. Shastri, A. Dangi, A. Jeyaseelan, S. Dutta, R. Pratap, Fluid density sensing using piezoelectric micromachined ultrasound transducers, IEEE Sens. J. 20 (2020) 6802–6809, https://doi.org/10.1109/JSEN.2019.2936469
[7] X. Lv, Y. Luo, Y. Zheng, C. Dong and M. Deng, The Body Fluid Density Sensor Based on Ultrasonic Wave, 2006 IEEE International Conference on Information Acquisition, (2006), 727–731, https://doi.org/10.1109/ICIA.2006.305818.
[8] Siyuan Zhang, Huiling Li, Huaiyong Li, Shihong Zhou, Xueqiang Cao, Calculation of the bulk modulus of simple and complex crystals with the chemical bond method, J. Phys. Chem. B 111 (2007) 1304–1309, https://doi.org/10.1021/jp0651539
[9] Yao Lu, Menglun Zhang, Hongxiang Zhang, Yuan Jiang, Hao Zhang, Wei Pang, Microfluidic bulk-modulus measurement by a nanowavelength longitudinal-acoustic-wave microsensor in the nonreflective regime, Phys. Rev. Appl. 11 (2019) 044091, https://doi.org/10.1103/PhysRevApplied.11.044091
[10] J.C. Andle, J.F. Vetelino, Acoustic wave biosensors, Sens. Actuators A Phys. 44 (1994) 167–176, https://doi.org/10.1016/0924-4247(94)00801-9
[11] Moussa Hoummady, Andrew Campitelli, Wojtek Wlodarski, Acoustic wave sensors: design, sensing mechanisms and applications, Smart Mater. Struct. 6 (1997) 647–657, https://doi.org/10.1088/0964-1726/6/6/001

[12] A. Mujahid, A. Afzal, F.L. Dickert, An overview of high frequency acoustic sensors-QCMs, SAWs and FBARs-chemical and biochemical applications, Sensors 19 (2019) 4395, https://doi.org/10.3390/s19204395
[13] Harmeet Bhugra, Gianluca Piazza, Piezoelectric MEMS Resonators, Springer, 2017, https://doi.org/10.1007/978-3-319-28688-4
[14] Y.Q. Fu, J.K. Luo, N.T. Nguyen, A.J. Walton, A.J. Flewitt, X.T. Zu, Y. Li, G. McHale, A. Matthews, E. Iborra, H. Du, W.I. Milne, Advances in piezoelectric thin films for acoustic biosensors, acoustofluidics and lab-on-chip applications, Prog. Mater. Sci. 89 (2017) 31–91, https://doi.org/10.1016/j.pmatsci.2017.04.006
[15] S. Jose, A.B. M. Jansman and R.J. E. Hueting, A design procedure for an acoustic mirror providing dual reflection of longitudinal and shear waves in Solidly Mounted BAW Resonators (SMRs), 2009 IEEE International Ultrasonics Symposium, (2009), 2111–2114, https://doi.org/10.1109/ULTSYM.2009.5442065.
[16] L. García-Gancedo, J. Pedrós, E. Iborra, M. Clement, X.B. Zhao, J. Olivares, J. Capilla, J.K. Luo, J.R. Lu, W.I. Milne, A.J. Flewitt, Direct comparison of the gravimetric responsivities of ZnO-based FBARs and SMRs, Sens. Actuators B Chem. 183 (2013) 136–143, https://doi.org/10.1016/j.snb.2013.03.085
[17] T. Baron, E. Lebrasseur, F. Bassignot, G. Martin, V. Pétrini, S. Ballandras, High-overtone bulk acoustic resonator, in: Marco G. Beghi (Ed.), Modeling and Measurement Methods for Acoustic Waves and for Acoustic Microdevices, IntechOpen, 2013, , https://doi.org/10.5772/56175
[18] Y. Yamakawa, K. Sano, R. Karasawa and T. Yanagitani, Broadband frequency viscosity measurement using low TCF shear mode resonators consisting of C-axis tilted scaln thin film on thick at-cut quartz plate, 19th International Conference on Solid-State Sensors, Actuators and Microsystems (TRANSDUCERS), 2017, 2135–2138, https://doi.org/10.1109/TRANSDUCERS.2017.7994497.
[19] W. Xu, J. Appel, J. Chae, Real-time monitoring of whole blood coagulation using a microfabricated contour-mode film bulk acoustic resonator, J. Microelectromech. Syst. 21 (2012) 302–307, https://doi.org/10.1109/JMEMS.2011.2179011
[20] A.J. Flewitt, J.K. Luo, Y.Q. Fu, L. Garcia-Gancedo, X.Y. Du, J.R. Lu, X.B. Zhao, E. Iborra, M. Ramos, W.I. Milne, ZnO based SAW and FBAR devices for bio-sensing applications, J. Non-Newton. Fluid Mech. 222 (2015) 209–216, https://doi.org/10.1016/j.jnnfm.2014.12.002
[21] L.M. Dorojkine, V.V. Volkov, V.S. Doroshenko, A.A. Lavrenov, D.A. Mourashov, I.A. Rozanov, Thin-film piezoelectric acoustic sensors. Application to the detection of hydrocarbons, Sens. Actuators B Chem. 44 (1997) 488–494, https://doi.org/10.1016/S0925-4005(97)00260-8
[22] G.D. Mansfeld, Theory of high overtone bulk acoustic wave resonator as a gas sensor, 13th International Conference on Microwaves, Radar and Wireless Communications, 2, 2000, 469–472, https://doi.org/10.1109/MIKON.2000.913971.
[23] J.C. Kuo, J.T. Hoople, M. Abdelmejeed, M. Abdel-moneum and A. Lal, 64-Pixel solid state CMOS compatible ultrasonic fingerprint reader, IEEE 30th International Conference on Micro Electro Mechanical Systems (MEMS), 2017, 9–12, https://doi.org/10.1109/MEMSYS.2017.7863326.
[24] M. Abdelmejeed et al., Monolithic 180nm CMOS Controlled GHz Ultrasonic Impedance Sensing and Imaging, 2019 IEEE International Electron Devices Meeting (IEDM), 2019, 34.3.1–34.3.4., https://doi.org/10.1109/IEDM19573.2019.8993623.
[25] C. Verdier, P.Y. Longin, M. Piau, Dynamic shear and compressional behavior of polydimethylsiloxanes: Ultrasonic and low frequency characterization, Rheol. Acta 37 (1998) 234–244, https://doi.org/10.1007/s003970050111
[26] Y. Lu, H. Zhang, Y. Jiang, H. Zhang, W. Pang and M. Zhang, Bulk modulus measurement of microfluidics by longitudinal bulk acoustic wave sensors, 2018 IEEE Micro Electro Mechanical Systems (MEMS), (2018), 854–857, https://doi.org/10.1109/MEMSYS.2018.8346690.
[27] PiezoMUMPs Reference Material, Design rules, ⟨http://www.memscap.com/products/mumps/piezomumps/reference-material⟩, 2012, (accessed 2 July 2021).
[28] Lawrence E. Kinsler, Austin R. Frey, Alan B. Coppens, James V. Sanders, Fundamentals of Acoustics, 4th edition, John Wiley & Sons Inc, 2000.
[29] J. Yanez, F. Torres, A. Uranga and N. Barniol, A feasibility study of AlN ultrasonic transducers fabrication using the multi-user PiezoMUMPs process for fingerprint scanning at GHz range, 15th Conference on Ph.D Research in Microelectronics and Electronics (PRIME), 2019, 293–296. https://doi.org/10.1109/PRIME.2019.8787767.
[30] G. Fan, J. Li, C. Wang, Design and analysis of MEMS linear phased array, Micromachines 7 (2016) 8, https://doi.org/10.3390/mi7010008
[31] J.F. Rosenbaum, Bulk Acoustic Wave Theory and Devices, Artech House, 1988.
[32] S. Ballandras, T. Baron, E. Lebrasseur, G. Martin, D. Gachon, A. Reinhardt, P. Lassagne, J. Friedt, L. Chommeloux, D. RabusHigh, High Overtone Bulk Acoustic Resonators: application to resonators, filters and sensors, Acoustics 2012 (2012) 3111–3117.
[33] J. Yanez, E. Ledesma, A. Uranga and N. Barniol, Improved Electromechanical Transduction for PiezoMUMPS HBAR Impedance Sensors, 2020 Joint Conference of the IEEE International Frequency Control Symposium and International Symposium on Applications of Ferroelectrics (IFCS-ISAF), 2020, 1–5. https://doi.org/10.1109/IFCS-ISAF41089.2020.9234913.
[34] J. Yanez, A. Uranga and N. Barniol, Multi-frequency thin film HBAR microsensor for acoustic impedance sensing over the GHz range, 21st International Conference on Solid-state sensors, Actuators and Microsystems (Transducers), 2021, 1347–1350, https://doi.org/10.1109/Transducers50396.2021.9495750.
[35] J. Kestin, J.H. Whitelaw, The viscosity of dry and humid air, Int. J. Heat Mass Transf. 7 (1964) 1245–1255, https://doi.org/10.1016/0017-9310(64)90066-3
[36] Cramer Owen, The variation of the specific heat ratio and the speed of sound in air with temperature, pressure, humidity, and CO_2 concentration, J. Acoust. Soc. Am. 93 (1993) 2510–2516, https://doi.org/10.1121/1.405827
[37] T.S. Khasanshin, A.A. Aleksandrov, Thermodynamic properties of ethanol at atmospheric pressure, J. Eng. Phys. 47 (1984) 1046–1052, https://doi.org/10.1007/BF00873717
[38] J. Tong, M.J.W. Povey, X. Zou, B. Ward, C.P. Oates, Speed of sound and density of ethanol-water mixture across the temperature range 10 to 50 degrees Celsius, J. Phys. Conf. Ser. 279 (2011), https://doi.org/10.1088/1742-6596/279/1/012023
[39] I.S. Khattab, F. Bandarkar, M.A.A. Fakhree, A. Jouyban, Density, viscosity, and surface tension of water+ethanol mixtures from 293 to 323K, Korean J. Chem. Eng. 29 (2012) 812–817, https://doi.org/10.1007/s11814-011-0239-6
[40] 3M Fluorinert Electronic Liquid FC-70, ⟨https://www.3m.com/3M/en_US/p/d/b40045189/⟩, 2021, (accessed 2 July 2021).
[41] L.M. Krutyanskiy, F. Zoueshtiagh, P. Pernod, P. Shirkovskiy, A.P. Brysev, Separation of two fractions of immiscible liquids by ultrasound in microgravity, Phys. Wave Phenom. 25 (2017) 151–155, https://doi.org/10.3103/S1541308X17020133
[42] J.B. Patterson, E.C. Morris, Measurement of absolute water density, 1 °C to 40 °C, Metrologia 31 (1994) 277–288, https://doi.org/10.1088/0026-1394/31/4/001
[43] Nykolai Bilaniuk, George S.K. Wong, Speed of sound in pure water as a function of temperature, J. Acoust. Soc. Am. 93 (1993) 1609–1612, https://doi.org/10.1121/1.406819
[44] Joseph Kestin, Mordechai Sokolov, A.Wakeham William, Viscosity of liquid water in the range −8 °C to 150 °C, J. Phys. Chem. Ref. Data 7 (1978) 941–948, https://doi.org/10.1063/1.555581
[45] Cheng Nian-Sheng, Formula for the viscosity of a glycerol–water mixture, Ind. Eng. Chem. Res. 47 (2008) 3285–3288, https://doi.org/10.1021/ie071349z
[46] Ana P.V. Egas, Nieves M.C. Talavera-Prieto, Abel G.M. Ferreira, Jaime B. Santos, M.ário J. Santos, Zaida L. Almeida, Isabel M.A. Fonseca, Speed of sound and derived thermodynamic properties of glycerol, J. Chem. Thermodyn. 156 (2021) 106367, https://doi.org/10.1016/j.jct.2020.106367
[47] M. Abdelmejeed, J. Kuo, A. Ravi and A. Lal, CMOS Controlled Ghz Ultrasonic Impedance Imager, 20th International Conference on Solid-State Sensors, Actuators and Microsystems & Eurosensors XXXIII (TRANSDUCERS & EUROSENSORS XXXIII), 2019, 57–60, https://doi.org/10.1109/TRANSDUCERS.2019.8808493.
[48] C.édric Ayela, Liviu Nicu, Micromachined piezoelectric membranes with high nominal quality factors in newtonian liquid media: a Lamb's model validation at the microscale, Sens. Actuators B Chem. 123 (2007) 860–868, https://doi.org/10.1016/j.snb.2006.10.048
[49] H. Antlinger, S. Clara, R. Beigelbeck, S. Cerimovic, F. Keplinger, B. Jakoby, Sensing the characteristic acoustic impedance of a fluid utilizing acoustic pressure waves, Sens. Actuators A Phys. 186 (2012) 94–99, https://doi.org/10.1016/j.sna.2012.02.050
[50] S. Cerimovic, R. Beigelbeck, H. Antlinger, J. Schalko, B. Jakoby, F. Keplinger, Sensing viscosity and density of glycerol–water mixtures utilizing a suspended plate MEMS resonator, Microsyst. Technol. 18 (2012) 1045–1056, https://doi.org/10.1007/s00542-012-1437-9
[51] Marc Meyers and Krishan Chawla. Mechanical Behavior of Materials, 2nd Edition, Cambridge University Press, 2009.
[52] C. Verdier, M. Piau, Acoustic wave propagation in two-phase viscoelastic fluids: the case of polymer emulsions, J. Acoust. Soc. Am. 101 (4) (1997) 1868–1876, https://doi.org/10.1121/1.418238
[53] D.J. Dos Santos, D.J. Carastan, L.B. Tavares, G.F. Batalha, Polymeric Materials Characterization and Modeling, Comprehensive Materials Processing, 2 (2014), pp. 37–63, https://doi.org/10.1016/B978-0-08-096532-1.00205-3

Jesus Yanez received both the B.Eng. degree in telecommunication and electronics engineering and the M.Sc. degree in Computer engineering from the National Polytechnic Institute, México, in 2008 and 2014 respectively. He is currently pursuing the Ph.D. degree in electronics engineering at Universitat Autònoma de Barcelona, Spain. His research interest includes piezoelectric acoustic transducers for ultrasonic sensor applications.

Arantxa Uranga received the degrees in physics and electronics engineering from Valladolid University, Spain, in 1994 and 1996, respectively, and the Ph.D. degree in electronics engineering from the Universitat Autònoma de Barcelona, Spain, in 2001. Since 1996, she has been with the Department of Electronics Engineering, Universitat Autònoma de Barcelona, where she is currently an Associate Professor. Her research interests include the design and implementation of CMOS integrated circuitry intended to sense the movement of MEMS-NEMS resonators; the implementation of

self-sustained oscillators based on MEMS, and the implementation of CMOS circuitry to excite and sense piezoelectric micromachined ultrasound transducers (PMUTs).

Núria Barniol received the Ph.D. degree in physics from the Universitat Autònoma de Barcelona (UAB), Spain, in 1992. She is a Full Professor with the Department of Electronics Engineering, UAB. She has been working for the last 20 years with MEMS resonators and their integration within CMOS technologies focused on the reduction of dimensions towards nanoelectromechanical devices with optimized CMOS conditioning circuitry. She has coauthored more than 100 research articles and 200 peer-reviewed conferences. Her research interests include the study of novel piezoelectrical micro/nanometric ultrasonic transducers, their integration with CMOS toward efficient biometrics systems and exploitation of non-linear NEMS resonators.